Dalton Transactions

Modulation of CO2 Adsorption in Novel Pillar-layered MOFs Based on Carboxylate-pyrazole Flexible Linker

Journal:	*Dalton Transactions*
Manuscript ID	DT-ART-09-2020-003166.R1
Article Type:	Paper
Date Submitted by the Author:	21-Jan-2021
Complete List of Authors:	Lancheros, Andres; Pontificia Universidad Catolica de Chile, Química Inorgánica Goswami, Subhadip; Northwestern University, Chemistry Mian, Mohammad; Northwestern University, Department of Chemistry Zhang, Xuan; Northwestern University, Zárate, Ximena; Universidad Autónoma de Chile Farha, Omar; Northwestern University, Department of Chemistry Schott, Eduardo; Pontificia Universidad Católica de Chile, Facultad de Química Hupp, Joseph; Northwestern University, Chemistry

Modulation of CO_2 Adsorption in Novel Pillar-layered MOFs Based on Carboxylate-pyrazole Flexible Linker

Andrés Lancheros[1,2,3], Subhadip Goswami[3], Mohammad Rasel Mian[3], Xuan Zhang[3], Ximena Zarate[4], Eduardo Schott[1,2]*, Omar K. Farha[3], Joseph T. Hupp[3]*

[1]Departamento de Química Inorgánica, Facultad de Química y Farmacia, Centro de Energía UC, Centro de Investigación en Nanotecnología y Materiales Avanzados CIEN-UC, Pontificia Universidad Católica de Chile, Avenida Vicuña Mackenna 4860, Santiago, Chile
[2]ANID -Millennium Science Initiative Program- Millennium Nuclei on Catalytic Process Towards Sustainable Chemistry (CSC), Chile
[3]Department of Chemistry and International Institute for Nanotechnology, Northwestern University, 2145 Sheridan Road, Evanston, Illinois 60208, United States
[4] Instituto de Ciencias Químicas Aplicadas, Theoretical and Computational Chemistry Center, Facultad de Ingeniería, Universidad Autónoma de Chile, Av. Pedro de Valdivia 425, Santiago, Chile.

ABSTRACT

Metal-organic frameworks (MOFs) have attracted significant attention as sorbents due to their high surface area, tunable pore volume and pore size, coordinatively unsaturated metal sites, and ability to install desired functional groups by post-synthetic modification. Herein, we report three new MOFs with pillar-paddlewheel structures that have been synthesized solvothermally from the mixture of the carboxylate-pyrazole flexible linker (H_2L), 4,4-bipyridine (BPY)/triethylenediamine (DABCO), and Zn(II)/Cu(II) ions. The MOFs obtained, namely [Zn^{II}(L)BPY], [Cu^{II}(L)BPY], and [Cu^{II}(L)DABCO], exhibit two-fold interpenetration and dinuclear paddle-wheel nodes. The Zn(II)/Cu(II) cations are coordinated by two equatorial L linkers that result in two-dimensional sheets which in turn are pillared by BPY or DABCO in the perpendicular direction to obtain a neutral three-dimensional framework that shows one-dimensional square channels. The three pillar-layered MOFs were characterized as microporous materials showing high crystalline stability after activation at 120ºC and CO_2 adsorption. All MOFs contain uncoordinated Lewis basic pyrazole nitrogen atoms in the framework which have an affinity toward CO_2 and hence could potentially serve as CO_2 adsorption material. The CO_2 uptake capacity was initially enhanced by replacing Zn with Cu and then replacing the pillar, going from BPY to DABCO. Overall, all the MOFs exhibit low isosteric heat (Q_{st}) of adsorption which signifies an advantage due to the energy required for the adsorption and regeneration processes.

INTRODUCTION

In recent decades, with an increasing demand for global energy and concomitant usage of fossil fuels, the concentration of CO_2 in the atmosphere has increased gradually. As this gas is one of the leading causes of the greenhouse effect and, therefore, global warming, CO_2 adsorption, or conversion had been considered a research topic with high priority.[1,2] The large-scale conventional method for CO_2 capture from exhaust streams from power plants, and subsequent controlled release of the captured CO_2, involves the use of aqueous amine solvents as reversibly chemically reactive sorbents.[2,3] This approach, while demonstrably functional, has not been widely adopted. As an alternative to reversible chemical binding to corrosive amine-containing liquids, physisorption to high-area porous materials (solids), has many potential advantages. They include higher adsorption capacity, lower desorption energy, and ease of handling.[3,4]

Different types of solid adsorbers have been investigated for CO_2 adsorption[5], including carbonaceous materials: activated carbon,[6,7] carbon nanotubes,[8,9], and graphene[10,11]; as well as zeolites[12] and ordered mesoporous silica.[13] Nevertheless, in recent years metal-organic frameworks (MOFs) which are a class of crystalline porous materials built from metal nodes and organic linkers connected by coordination bonds,[14,15] have been recognized as one of the most promising alternatives for selective gas adsorption due to their high surface area, large pore volumes, adaptable pore size, ability to create an unsaturated metal co-ordination sites and installation of desired functional groups by post-synthetic modification.[16,17]

In order to improve the CO_2 adsorption capacity and selectivity using MOFs, three main strategies have been reported:[18] (1) incorporation of coordinatively unsaturated (open) metal sites, which allows the interaction with CO_2 molecules providing high adsorption at very low pressures and selectivity of CO_2 over

N_2,[19,20] (2) decoration with Lewis basic sites- this approach involves the use or functionalization of organic linkers with polar groups containing nitrogen or hydroxyl because of the strong interactions with CO_2; examples of those groups are; primary, secondary or tertiary amines, tetrazole, triazine, imidazole, and pyrazole,[21,22] and (3) to use flexible linkers with tunable porosity as a result of host-guest interactions inducing guest-responsive dynamic behavior, this is a unique advantage for gas storage and separation.[23,24,25]

However, the synthesis of MOFs using flexible or large linkers (third strategy) may still be a challenge.[26,27] In many cases, large porous MOFs collapse quickly after removal of the guest solvent molecules, turning them into amorphous non-porous material.[28] Pillar-layered MOFs have surged as an effective and straightforward strategy to retain porosity by avoiding structural collapse. This approach consists of building three-dimensional (3D) porous frameworks from 2D layers (formed by multitopic carboxylic acid linkers and metal node) by coordination of dipyridyl pillaring linkers with unsaturated metal nodes to get more stable structures.[29] Pillar-layered MOFs show tunable pore volume or window size depending on the length of the pillar or the carboxylate ligands that form the 2D sheets which result in distinct properties.[26,30] Also, pillar-layered MOFs allow post-synthetic modification by introducing functional groups into the pores to get desired properties without changing the network topology.[29,30]

Here, we present the synthesis, characterization, and CO_2 adsorption performances of three new pillar-layered MOFs based on carboxylate-pyrazole flexible linker (H_2L), with Zn (II) or Cu (II) metal nodes, and 4,4'-bipyridine (BPY) or triethylenediamine (DABCO) as pillaring ligands. Here we have used carboxylate-pyrazole flexible linker H_2L based on the following considerations: the carboxylate ligands represent one of the most studied types of linkers due to their ability to make strong metal-carboxylate bonds which have allowed to obtain a large family of MOFs [31,32,33,34]; the pyrazole group is a softer base than the carboxylate, therefore it does not participate in the formation of the MOF, instead, it presents the opportunity to use the nitrogens of pyrazole group for the adsorption of CO_2. Additionally, the flexibility of the linker could be advantageous for gas storage/separation. The three new MOFs obtained are three-dimensional interpenetrated microporous materials with pillared-paddlewheel type topology. Although the frameworks exhibit similar topology, but differ in porosity, thermal stability, and CO_2 adsorption properties, depending on the choice of the metal ions and dipyridyl linkers. The difference in CO_2 uptake ability was further verified by DFT calculations showing higher interaction energy between CO_2 and MOF pores for [Cu^{II}(L)DABCO].

EXPERIMENTAL SECTION

Materials

All reagents and solvents were commercially purchased from commercial suppliers and used without further purification. Acetylacetone (≥99%), formaldehyde (37%), magnesium sulfate anhydrous (≥98%), acetic acid (≥99.7%), terephthalaldehyde (99%) 4,4′-bipyridine (98%), diethyl ether (≥99%), ethyl acetate (99.8%), acetic acid (≥99.7%) and triethylenediamine (≥99%) were purchased from Sigma Aldrich. 4-hydrazinobenzoic acid (97%) was purchased from Fisher Chemical. N,N-Dimethylformamide (DMF) (99%) was purchased from Acros organics, copper(II) nitrate trihydrate (99%) was purchased J.T. Baker, and zinc(II) nitrate hexahydrate (98%) was purchased from Strem Chemicals.

Synthesis of the linker (H_2L)

The structure of the linker (H_2L) is shown in **Figure 1** and was synthesized in two steps according to the previous reports,[35] details of the synthesis, and structural characterizations are provided in the Supporting Information (**Scheme S1**).

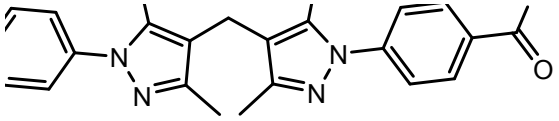

Figure 1. Chemical structure of the linker H_2L

Synthesis [Zn^{II}(L)BPY] single crystal

The mixture of H_2L (111.05 mg, 0.25 mmol, 1 equiv.) and 4,4′-bipyridine (19.5 mg, 0.125 mmol, 0.5 equiv.) in DMF (1.5 mL) was sonicated until all the solids were dissolved. In another vial, $Zn(NO_3)_2{\cdot}6H_2O$ (47.30 mg, 0.25 mmol, 1 equiv.) was dissolved in DMF (1.5 mL). The solutions were mixed in a 2-dram vial, capped, and placed in an oven preheated to 120 °C for 72 hours. After cooling down to room temperature, the reaction mixture was centrifuged at 8500 rpm for 10 minutes and the supernatant was poured out. The solid was washed sequentially with DMF (10 mL x 3) and acetone (10 mL x 3). Finally, it was soaked with acetone overnight, centrifuged, and dried in air to give a light-yellow powder.

Synthesis [Cu^{II}(L)BPY] single crystal

The linker H_2L (111.05 mg, 1 mmol, 1 equiv.) and 4,4′-bipyridine (19.5 mg, 0.125 mmol, 0.5 equiv.) were dissolved in DMF (1.5 mL) by sonication for 10 minutes. In a separate vial, $Cu(NO_3)_2{\cdot}3H_2O$ (60.40 mg, 0.25 mmol, 1 equiv.) was entirely dissolved in DMF (1.5 mL). The copper solution was then added to the ligands solution and sonicated until the reaction mixture was homogenized. The resulting mixture was capped and heated at 120°C in an oven for 48 hours before being cooled to room temperature. The light-green powder product was collected by centrifugation and washed with DMF (10 mL x 3) and acetone (10 mL x 3). Then, the material was immersed in acetone (10 mL) and kept at room temperature overnight. To obtain the product, this mixture was centrifuged and air-dried.

Synthesis [Cu^{II}(L)DABCO] single crystal

In a 3-dram vial, the linker H_2L (111.05 mg, 0.25 mmol, 1 equiv.), triethylenediamine (DABCO) (11.4 mg, 0.125 mmol, 0.5 equiv.) and DMF (4.0 mL) were added. The mixture was sonicated until all the solids were dissolved. On the other hand, $Cu(NO_3)_2{\cdot}3H_2O$ (60.40 mg, 0.25 mmol, 1 equiv.) was dissolved in DMF (3.5 mL), which were placed in a 2-dram vial. The solutions were mixed in a 3-dram vial, capped, and placed in an oven preheated to 120 °C for 72 hours. After cooling down to room temperature, the reaction mixture was centrifuged at 8500 rpm for 10 minutes and the upper solvent was poured out. The solid was washed three times with DMF (10 mL) followed by three times with acetone (10 mL) every two hours. Finally, it was soaked with acetone overnight, centrifuged, and dried in air to give a green powder.

Physical measurements

Single-crystal X-ray crystallography. The data of [Zn^{II}(L)BPY], [Cu^{II}(L)BPY], and [Cu^{II}(L)DABCO] were collected at 100 K on a 'Bruker APEX-II CCD' diffractometer with a MoKα (λ = 0.71073 Å) microfocus X-ray source. The single crystal was mounted on MicroMesh (MiTeGen) with paratone oil. The structures were determined by intrinsic phasing (SHELXT 2018/2)[36] and refined by full-matrix least-squares refinement (SHELXL-2018/3)[37] using the Olex2[38] software packages. The refinement results are summarized in Table S1. Crystallographic data for the [Cu^{II}(L)BPY], [Zn^{II}(L)BPY] and [Cu^{II}(L)DABCO] structures in CIF format have been deposited in the Cambridge Crystallographic Data Centre (CCDC) under deposition numbers CCDC-2027569, 2027570, and 2027578, respectively. The data can be obtained free of charge via www.ccdc.cam.ac.uk/data_request/cif (or from the Cambridge Crystallographic Data Centre, 12 Union Road, Cambridge CB2 1EZ, U.K.).

Powder X-ray Diffraction (PXRD). PXRD patterns of MOFs were recorded at room temperature on a STOE-STADI-MP powder diffractometer equipped with an asymmetrically curved Germanium monochromator (CuKα1 radiation, λ = 1.54056 Å) and one-dimensional silicon strip detector (MYTHEN2 1K from DECTRIS). The line focused Cu X-ray tube was operated at 40 kV and 40 mA. The activated MOF powder was packed in a 3 mm metallic mask and sandwiched between two polyimide layers of tape and measured in transmission geometry in a rotating holder. Intensity data from 1 to 34 degrees 2θ were collected over 7 minutes. The instrument was calibrated against a NIST Silicon standard (640d) prior the measured.

Thermogravimetric Analysis (TGA). TGA was performed on a TGA/DCS 1 system (Mettler-Toledo AG, Schwerzenbach, Switzerland), which runs on a PC with STARe software. Samples were heated from 25 to 600 °C at a rate of 10 °C/min under nitrogen with a flow rate of 20 mL/min.

Fourier-Transform Infrared Spectroscopy (FTIR). Measurements of FTIR were carried out on a Fourier transform spectrometer SHIMADZU IRTracer-100. Absorption spectra at a resolution of one data point per 8 cm^{-1} were obtained in the region between 4000 cm^{-1} and 350 cm^{-1}. All spectra were recorded at room temperature using KBr disc cell. 16 scans were collected, fourier-transformed and averaged for each measurement. Spectral analysis was performed with Labsolution IR software from SHIMADZU corporation.

N_2 adsorption and desorption isotherms. All the measurements were performed on a Micromeritics Tristar II 3020 (Micromeritics, Norcross, GA) instrument at 77 K. Pore-size distributions were obtained using NL-DFT model with N2 kernel. Before each run, all the MOF samples were activated by heating 120 °C for 16 h under a high dynamic vacuum on a Smart Vacprep from Micromeritics. Around 50 mg of sample was used in each measurement and Brunauer–Emmett–Teller (BET) surface area was calculated in the region P/P_0 = 0.005–0.05.

CO_2 Sorption Measurements. The CO_2 adsorption experiment was performed with Micromeritics ASAP 2020 surface area analyzer. Approximately 50 mg of sample was used which previously was activated by heating 120°C under dynamic vacuum on a Smart Vacprep from Micromeritics until the outgassing rate was <5 μmHg/min. The different temperatures at which the measurements were taken, were maintained by using a Micromeritics Iso Controller.

Isosteric heats of the CO_2 adsorption (Q_{st}, Kj mol^{-1}) were determined according to the Clausius-Clapeyron equation (Eq. (1)), where T (K) is the temperature, R is the universal gas constant (R =8.314 J mol^{-1} K^{-1}), and C is a constant.[18,39]

$$(lnP)_N = -\frac{Q_{st}}{R}\frac{1}{T} + C \qquad Equation\ 1$$

Theoretical calculations.

Relativistic density functional theory[40] calculations were carried out by using the ADF 2018.02 code[41,42] incorporating scalar corrections via the ZORA Hamiltonian.[43, 44, 45] Triple-ξ Slater basis set[46] (STO-TZP) for valence electrons were employed together with the RPBE functional[47] with Grimme D3 dispersion correction.[48] The ground state equilibrium geometries were undertaken without any symmetry restrain, via the analytical energy gradient method implemented by Versluis and Ziegler.[49] The optimized geometries were proven to be minima in the potential energy surface (PES) by calculating the vibrational frequencies. The nature of the binding interaction is studied in the truncated representation of the MOF and the CO_2 adsorbed molecules through the Morokuma-Ziegler decomposition scheme. The binding energy was determined by applying a fragment approximation to the molecular structure and the decomposition of the interaction energy (ΔE_{Int}) among the fragments. Therefore, this compound was logically studied as two fragments that constitute the whole system: The truncated fragment of the MOF and the CO_2 molecules adsorbed on this structure. The interaction energy can be decomposed as: [50]

$$\Delta E_{Int} = \Delta E_{Elec} + \Delta E_{Pauli} + \Delta E_{Dis} + \Delta E_{Orb} \qquad Equation\ 2$$

The ΔE_{Pauli} refers to the Pauli repulsion (commonly known as exchange repulsion). This energy is responsible for any steric repulsion. The remaining three terms corresponds to the classical electrostatic interaction (ΔE_{Elec}), the dispersive contribution (ΔE_{Dis}), and the effect of the orbital interaction and polarization effects (ΔE_{Orb}). All these terms have a stabilizing contribution to the interaction energy.

RESULTS AND DISCUSSION

Crystal Structure analysis

In order to elucidate the structure of three frameworks, SCXRD measurements were acquired on crystals grown from metal salts and H_2L linker in the presence of additional BPY or DABCO pillar ligands with a molar ratio of 2:2:1 in anhydrous DMF at 120 °C. Light-yellow plate-like crystals for [Zn^{II}(L)BPY] and green plate-like crystals for both [Cu^{II}(L)BPY] and [Cu^{II}(L)DABCO] were obtained after three days. The crystal structure and crystallographic data are summarized in **Figure 2** and **Table S1**, respectively. Both [Zn^{II}(L)BPY] and [Cu^{II}(L)BPY] crystallize in the monoclinic space group C*2/m.* On the other hand, [Cu^{II}(L)DABCO] crystallizes in orthorhombic space group P*bcm* due to different lengths and shapes of the pillar linker. The asymmetric unit of three MOFs is constructed by a node, one L linker, and one BPY/DABCO molecule (**Figure 2**). The node is composed of two metal ions in paddle-wheel fashion with a metal⋯metal distance of 2.907 Å, 2.619 Å, and 2.926 Å for [Zn^{II}(L)BPY], [Cu^{II}(L)BPY], and [Cu^{II}(L)DABCO], respectively. Furthermore, the metal ions possess a square-pyramidal geometry completed by four oxygen atoms from four L linkers and a nitrogen atom from the pillar linker. The M–N and M–O distances were calculated to be 1.93–1.95 Å and 2.04–2.14 Å, respectively. Two L linkers in equatorial position form a two-dimensional (2D) sheets in *ab* plane through the connection of metal ions. The in-plane linker is bent around 64° from linear due to probably steric hindrance via bulky methylated groups as well as the flexibility of L linker. The 2D sheets are pillared by BPY/DABCO in the axial direction (along the *c* axis) to obtain a three-dimensional (3D) framework (**Figure 3**). All of them exhibit a two-fold interpenetrated structure. It is observed that two uncoordinated nitrogen atoms are present in each equatorial linker of all three frameworks that would be a good platform for CO_2 adsorption studies.

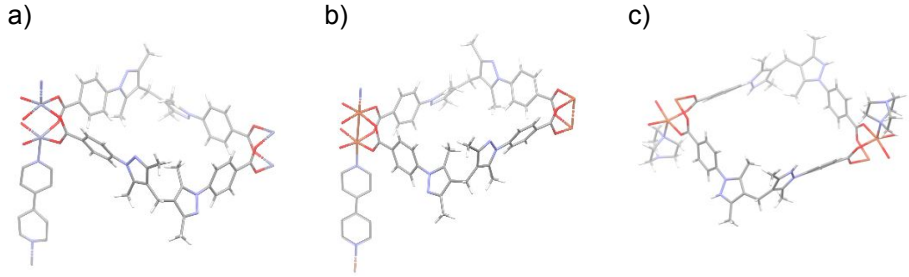

Figure 2. Coordination environment for a) Zn^{II} in [Zn^{II}(L)BPY], b) Cu^{II} in [Cu^{II}(L)BPY], and c) Cu^{II} in [Cu^{II}(L)DABCO]

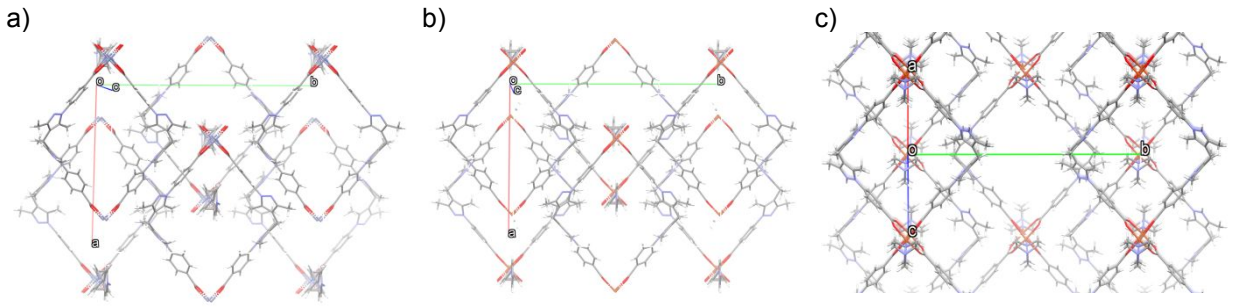

Figure 3. View of 2-fold interpenetrated 3D pillar-layered framework a) [Zn^{II}(L)BPY], b) [Cu^{II}(L)BPY], and c) [Cu^{II}(L)DABCO]

Powder X-ray diffraction (PXRD) and thermogravimetric analysis (TGA)

The crystallinity of the as-synthesized samples, after activation under dynamic vacuum at 120°C for 16 h and CO_2 adsorption were investigated by comparing the PXRD pattern after measurements with the simulated PXRD pattern obtained from the single-crystal structure data. As shown in **Figure 4** and **Figure S18**, the as-synthesized pillared-layered MOFs showed a high phase-purity and the crystallinity of the samples is maintained after activation at 120ºC for 16 h and after CO_2 absorption.

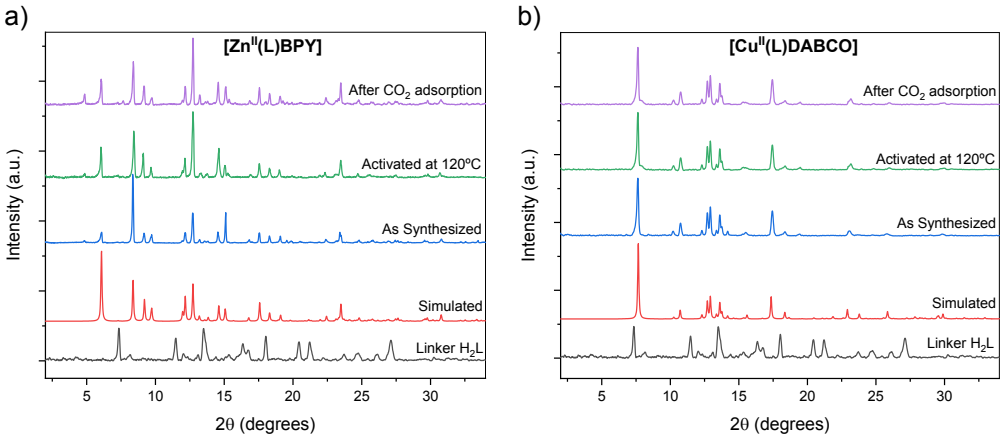

Figure 4. PXRD patterns for a) [Zn^{II}(L)BPY], and b) [Cu^{II}(L)DABCO]. Linker H_2L (black); simulated (red); as-synthesized (blue); activated at 120ºC x 16h (green); and after CO_2 adsorption (purple).

TGA curves for [Zn^{II}(L)BPY], [Cu^{II}(L)BPY], and [Cu^{II}(L)DABCO] showed that these pillar-layered MOFs are stable until 300ºC, 260ºC, and 250ºC, respectively (**Figures S19**). In all cases, the first weight loss (5%) between 30° and 250°C, corresponds to the release of guest molecules that had trapped in the framework. At lower temperatures, acetone and water (adsorbed from air) was removed that was used during washing of the samples after the synthesis, and DMF was released at higher temperatures (>150°C) which was used during the synthesis and washing. The [Zn^{II}(L)BPY] collapsed within the temperature range between 300°C and 470°C with a weight loss of ~65 % that could be attributed to the loss of the coordinating ligands. For [Cu^{II}(L)BPY] the collapse of the framework begins at 260°C and goes until 472°C, showing a similar weight loss of approximately ~65 %. The collapse of the [Cu^{II}(L)DABCO] occurred progressively from 250ºC until 472°C and showed a weight loss of ~58.50%.

Nitrogen (N_2) Adsorption Studies.

The evidence of the permanent porosity of [Zn^{II}(L)BPY], [Cu^{II}(L)BPY], and [Cu^{II}(L)DABCO], was obtained from N_2-adsorption/desorption measurements at 77K (**Figure 5** and **Figure S21**). Before the measurement, MOF samples were activated at 90°C for 1 hour and 120°C for 16 hours under a dynamic vacuum to remove the pore trapped solvent molecules. All the MOFs exhibit a type I isotherm, which is characteristic of microporous materials. In this type of isotherm, there is a high gas uptake at very low p/p_0 because of the adsorbate-adsorbent interactions in mainly narrow micropores.[51] The hysteresis loop of all the isotherms corresponds to type H4 and is often associated with narrow slit-like pores.[51,52] The estimated apparent Brunauer−Emmett−Teller (BET) surface areas are 290 m^2/g for [Zn^{II}(L)BPY], 430 m^2/g for [Cu^{II}(L)BPY], and 680 m^2/g for [Cu^{II}(L)DABCO]. The specific pore volumes also follow the same trend as BET surface area and recorded as 0.09 cm^3/g for [Zn^{II}(L)BPY], 0.18 cm^3/g for [Cu^{II}(L)BPY], and 0.31 cm^3/g for [Cu^{II}(L)DABCO]. The pore size distribution (PSD) (**Figure 6** and **Figure S21**) calculated from the nitrogen adsorption experiment reveals micropores with a diameter of 11 Å, 12 Å, and 8.6 Å for [Zn^{II}(L)BPY], [Cu^{II}(L)BPY], and [Cu^{II}(L)DABCO], respectively.

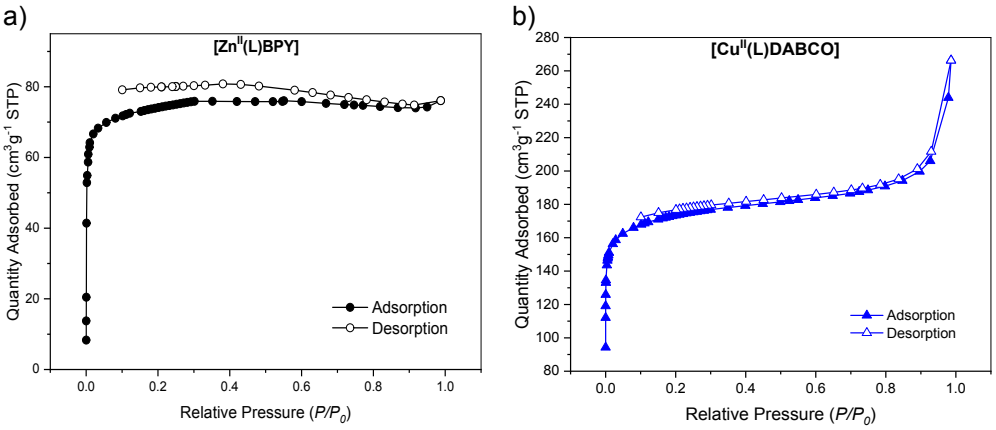

Figure 5. Nitrogen sorption isotherms at 77 K for a) [Zn^{II}(L)BPY], and b) [Cu^{II}(L)DABCO]

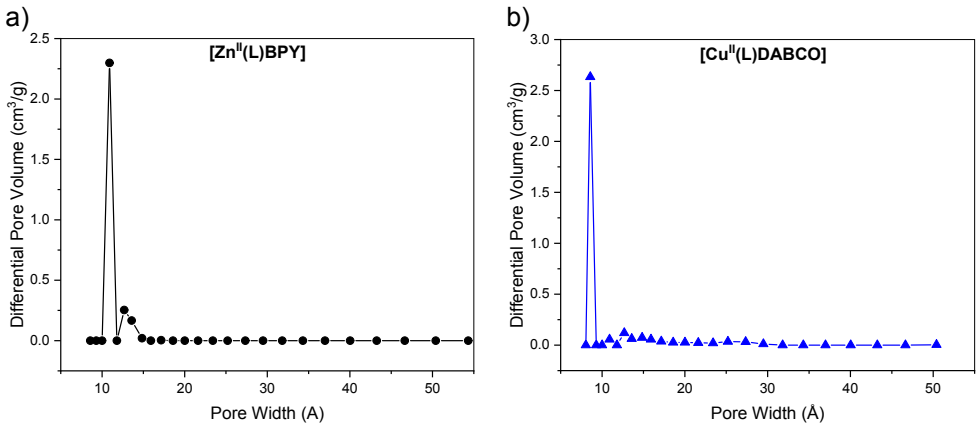

Figure 6. DFT calculated pore size distributions for a) [Zn^{II}(L)BPY], and b) [Cu^{II}(L)DABCO]

CO_2 Adsorption Studies.

Due to the availability of the uncoordinated nitrogen sites which can act as Lewis base and interact with the quadrupolar CO_2 (13.4×10^{-40} C m^2) we hypothesize, these MOFs will be beneficial for CO_2 uptake. The adsorption isotherms for CO_2 were determined at 195, 273, and 298 K, and results are presented in **Figure**

7 and **Table S2**. [Cu^{II}(L)DABCO] exhibits higher CO_2 uptake capacity than [Zn^{II}(L)BPY] and [Cu^{II}(L)BPY] regardless of the temperature at which it was measured. For all pillar-layered MOFs, we found that the CO_2 uptake decreases as temperature increases, typical behavior for an exothermic process where the CO_2 molecules are physisorbed on the surface of the MOFs.[4,53,54]

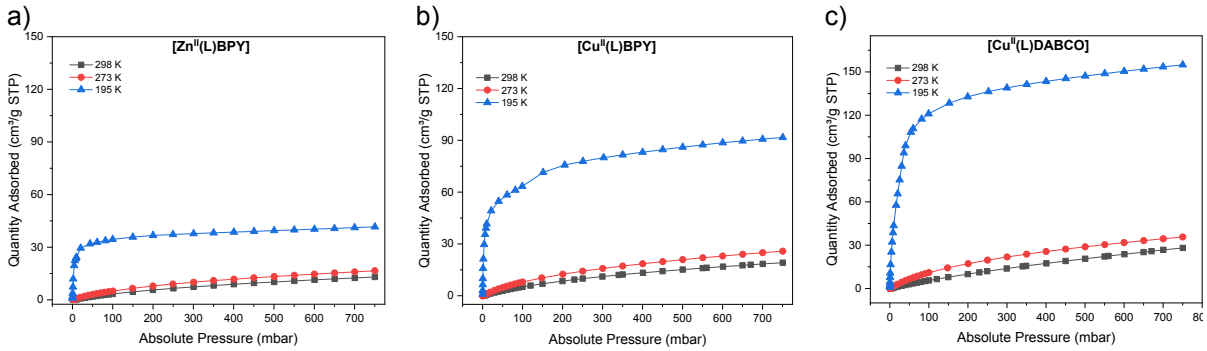

Figure 7. CO_2 adsorption isotherms at 195, 273 and 298 K for a) [Zn^{II}(L)BPY], b) [Cu^{II}(L)BPY], and c) [Cu^{II}(L)DABCO].

The CO_2 adsorption capacity at 298 K and 750 mbar for [Zn^{II}(L)BPY] was 2.68 wt% (13.5 cm^3 /g, 0.61 mmol/g), which increased to 3.39 wt% (17.1 cm^3/g, 0.77 mmol/g) when the temperature decreased to 273 K; at 195 K the amount of CO_2 adsorbed further increased to 8.35 wt% (42 cm^3/g, 1.90 mmol/g). The dramatic influence of the metal ion is observed towards CO_2 uptake capacity in a topologically similar MOF [Cu^{II}(L)BPY]. At 298 K and 750 mbar the uptake capacity was 3.94 wt% (20 cm^3/g, 0.89 mmol/g), at 273 K the adsorption increases until 5.28 wt% (26.69 cm^3/g, 1.20 mmol/g). Finally, the highest CO_2 uptake was of 18.2 wt% (92 cm^3/g, 4.12 mmol/g). When the pillaring linker 4,4'-bipyridine was replaced with a shorter linker DABCO in [Cu^{II}(L)DABCO], the CO_2 uptake capacity reaches to the maximum. The highest uptake, at 298 K and 750 mbar was 6.47 wt% (32.7 cm^3/g, 1.47 mmol/g), increasing to 7.20 wt% (36.4 cm^3/g, 1.64 mmol/g) at 273 K and finally, maximum uptake was 31.0 wt% (156 cm^3/g, 7.03 mmol/g) at 195 K.

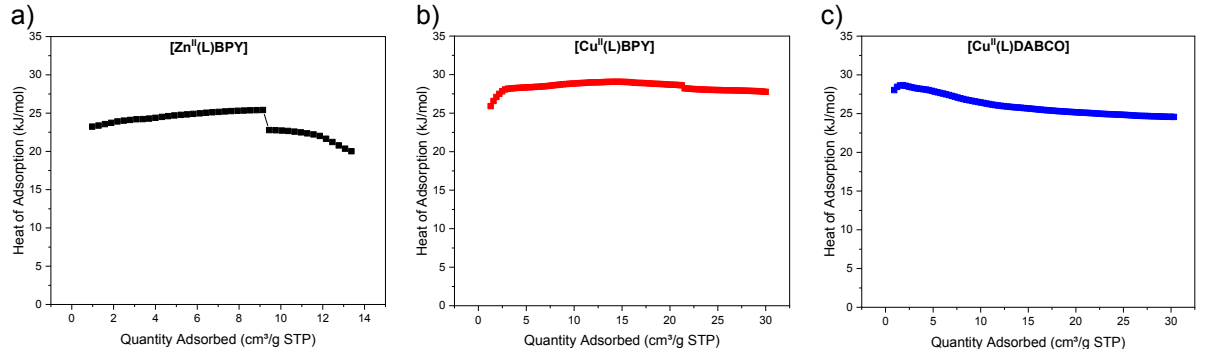

Figure 8. Heat of adsorption of CO_2 at different temperatures for a) [Zn^{II}(L)BPY] (We believe that the discontinuity at ~8 cm^3/g is a fitting artifact, rather than a real step-change) and b) [Cu^{II}(L)BPY], and c) [Cu^{II}(L)DABCO]

To understand further the interactions between CO_2 and the porous frameworks, the experimental isosteric heat (Q_{st}) of CO_2 adsorption was determined for the three pillar-MOFs and shown in **Figure 8** as a function of loading. The estimated value of Q_{st} for [Zn^{II}(L)BPY] was found to be 23.0 kJ/mol at zero coverage (Q_{st}^0), which is similar to the ultramicroporous MOFs without any active sites (20−25 kJ/mol).[55] At higher amounts of CO_2 adsorption, the obtained value of Q_{st} (approx. 20 kJ/mol) resembles that reported by Farrusseng and coworkers for IRMOF-3, which presents a functional amino group on the benzene 1,4-dicarboxylic linker.[56] The low Q_{st} found for [Zn^{II}(L)BPY] might allow CO_2 storage at more cost-effective prices, because of the reduced energy consumption and effective regeneration of the MOF.[57,58] [Cu^{II}(L)BPY] shown a value

of Q_{st}^{0} of 25.9 kJ/mol that means a relatively weak CO_2-adsorbent interaction; however, when the loading increases over 2 cm^3/g, the values rise to around 27-29 kJ/mol that was attributed to increasing CO_2-CO_2 interaction at higher loadings.[59] The calculated value of Q_{st}^{0} for [Cu^{II}(L)DABCO] was of 28.04 kJ/mol and then it decreases slightly as CO_2 loading increase. The enhancement can be attributed to the size differences between the pillars. Thus, DABCO led to smaller pore sizes (8.6 Å instead 11-12 Å for the BPY MOFs) which increase the interactions between CO_2 and the framework.[60] The obtained Q_{st} values suggests modest interaction of CO_2 with the MOF pores. Overall, we found that at zero coverage, the trend of Q_{st} values is clearly in accordance with the CO_2 uptake amounts following the trend: [Cu^{II}(L)DABCO] >[Cu^{II}(L)BPY] > [Zn^{II}(L)BPY].

Theoretical computations

In an effort to have more insight into the CO_2 adsorption behavior of these three MOFs, DFT calculations were performed over a truncated structure of the periodic structure. The studied fragment represents the section of interest of the MOFs that could be a potential interaction site with CO_2. Thus, two and four CO_2 molecules were included inside the cavity (see **Figure 9** and **Figure S22**) and the Morokuma-Ziegler energy decomposition was performed over the interaction (see **Table 1** and **Table S3**). The CO_2 molecules were optimized near and far from the free nitrogen present in the linker. As evident from the data, the estimated interaction energies are in accordance with the CO_2 adsorption capability of these materials, and these tendency is not dependent on the position where the CO_2 interacts with the MOF structure. Furthermore, [Zn^{II}(L)BPY] and [Cu^{II}(L)BPY] have a slight different interaction energy, which correlates well with the adsorption capability of the studied materials. While [Zn^{II}(L)BPY] shows the smallest interaction energy with CO_2, [Cu^{II}(L)DABCO] shows the largest interaction energy possibly due to the orbital energy contribution. Finally, the same trend of energy values and composition is observed when two or four CO_2 molecules are included inside the generated cavity of the studied MOF's.

Table 1. Morokuma-Ziegler EDA in Kcal/mol.

		ΔE_{Pauli}	ΔE_{Elec}	ΔE_{Orb}	ΔE_{Dis}	ΔE_{Int}
[Zn^{II}(L)BPY]	2 CO_2	12.6	-6.7	-2.9	-12.1	-9.1
	4 CO_2	44.0	-19.2	-9.2	-31.7	-16.0
[Cu^{II}(L)BPY]	2 CO_2	15.0	-7.9	-4.8	-14.1	-11.8
	4 CO_2	27.1	-13.6	-7.7	-26.1	-20.3
[Cu^{II}(L)DABCO]	2 CO_2	13.0	-6.5	-11.7	-12.1	-17.2
	4 CO_2	24.5	-12.0	-11.7	-25.1	-24.3

a)

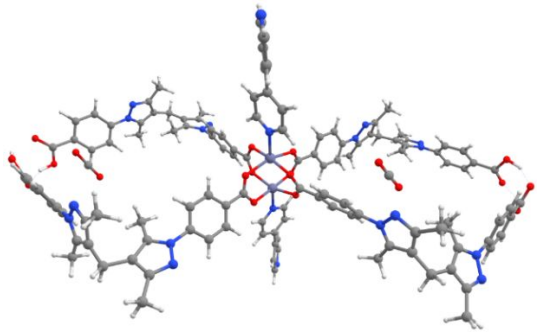

b)

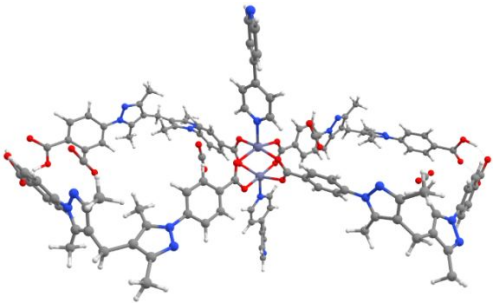

c)

d)

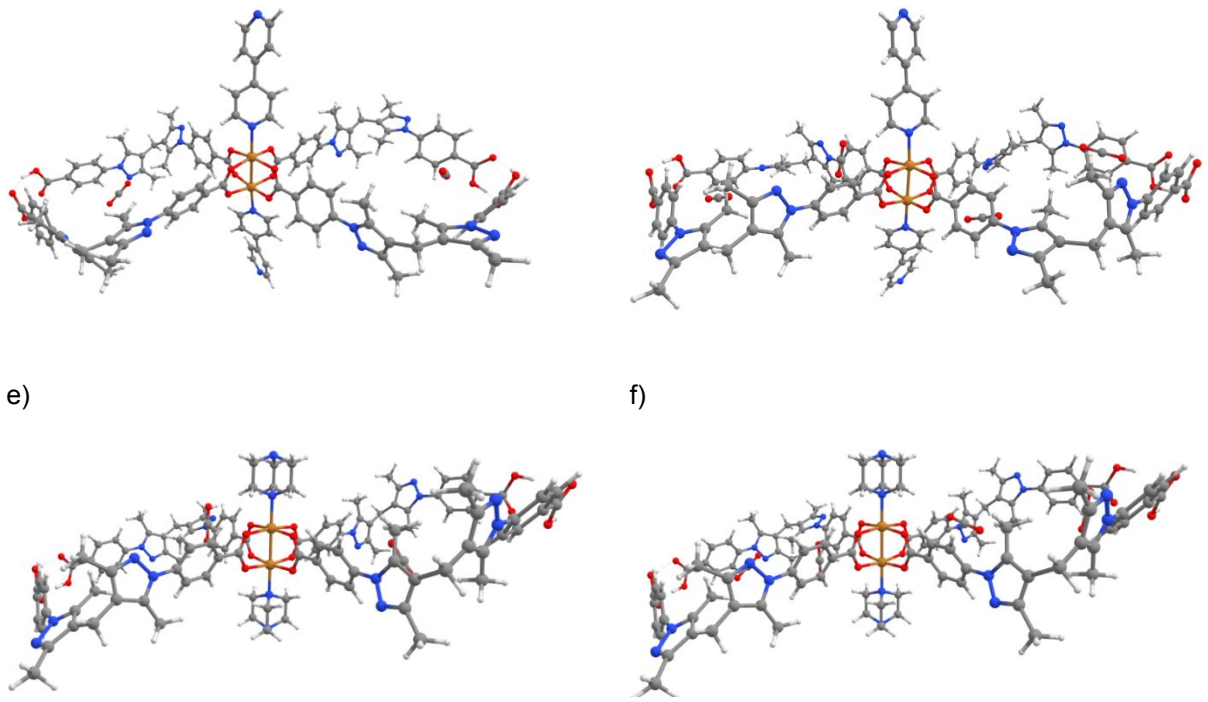

Figure 9. Studied MOFs and the adsorbed CO_2 molecules. [Zn^{II}(L)BPY] with a) 2 CO_2 molecules and b) 4 CO_2 molecules. [Cu^{II}(L)BPY] with c) 2 CO_2 molecules and d) 4 CO_2 molecules. [Cu^{II}(L)DABCO] with e)2 CO_2 molecules and f) 4 CO_2 molecules.

CONCLUSION

In summary, we have synthesized three new pillar-layered MOFs via the solvothermal synthesis method through the combination of carboxylate-pyrazole based flexible linker (L), and BPY or DABCO pillaring linker and either Zn^{2+} or Cu^{2+} metal salts. All of them exhibit two-fold interpenetration and nodes of the paddle-wheel type connected in the equatorial position to L linkers with the axial positions occupied by pillars. All MOFs are characterized as microporous materials with pore sizes of approximately 8-12 Å with high framework stability after activation at 120ºC for 16h and after CO_2 adsorption. All the MOFs show CO_2 uptake capacity, due, in part, to the presence of nitrogen-rich functionality within the 1D porous channels. The CO_2 uptake capacity was enhanced by replacing the Zn^{2+} in the nodes with Cu^{2+} and then replacing the pillar, going from BPY to DABCO. Further evidence of MOF Pores-CO_2 interaction came from DFT calculations. The energy of interaction between the MOFs and CO_2 was described in terms of its components for each studied material, and the results are in accordance with the experimental observation. In all cases, the relatively low Q_{st} for the CO_2 storage signifies a potential advantage due to the low energy required for the adsorption and regeneration.

Declarations of interest

OKF and JTH are equity holders in a start-up company, NuMat, that commercializes MOFs for gas storage and delivery.

ACKNOWLEDGMENTS

This work was supported by FONDECYT 1201880, 1180565, ANID/FONDAP/15110019 and ANID - Millennium Science Initiative Program- NCN17_040. At Northwestern this work was supported by the CBET SusChem program of the U. S. National Science Foundation, grant number 60044545.

REFERENCES

(1) Qasem, N. A. A.; Ben-Mansour, R.; Habib, M. A. An Efficient CO_2 Adsorptive Storage Using MOF-5 and MOF-177. *Appl. Energy* **2018**, *210* (October 2017), 317–326. https://doi.org/10.1016/j.apenergy.2017.11.011.

(2) Chen, C.; Jia, M.; Wang, G.; Li, X.; Li, S. High and Selective CO_2 Uptake in a Nitrogen-Rich Pillar-Layered Metal Organic Framework. *RSC Adv.* **2015**, *5* (127), 104932–104935. https://doi.org/10.1039/c5ra22144g.

(3) Samanta, A.; Zhao, A.; Shimizu, G. K. H.; Sarkar, P.; Gupta, R. Post-Combustion CO_2 Capture Using Solid Sorbents: A Review. *Ind. Eng. Chem. Res.* **2012**, *51* (4), 1438–1463. https://doi.org/10.1021/ie200686q.

(4) Landaverde-Alvarado, C.; Morris, A. J.; Martin, S. M. Gas Sorption and Kinetics of CO_2 Sorption and Transport in a Polymorphic Microporous MOF with Open Zn (II) Coordination Sites. *J. CO2 Util.* **2017**, *19*, 40–48. https://doi.org/10.1016/j.jcou.2017.01.029.

(5) Yu, C. H.; Huang, C. H.; Tan, C. S. A Review of CO_2 Capture by Absorption and Adsorption. *Aerosol Air Qual. Res.* **2012**, *12* (5), 745–769. https://doi.org/10.4209/aaqr.2012.05.0132.

(6) Wickramaratne, N. P.; Jaroniec, M. Activated Carbon Spheres for CO_2 Adsorption. *ACS Appl. Mater. Interfaces* **2013**, *5* (5), 1849–1855. https://doi.org/10.1021/am400112m.

(7) Singh, G.; Kim, I. Y.; Lakhi, K. S.; Srivastava, P.; Naidu, R.; Vinu, A. Single Step Synthesis of Activated Bio-Carbons with a High Surface Area and Their Excellent CO_2 Adsorption Capacity. *Carbon N. Y.* **2017**, *116*, 448–455. https://doi.org/10.1016/j.carbon.2017.02.015.

(8) Irani, M.; Jacobson, A. T.; Gasem, K. A. M.; Fan, M. Modified Carbon Nanotubes/Tetraethylenepentamine for CO_2 Capture. *Fuel* **2017**, *206*, 10–18. https://doi.org/10.1016/j.fuel.2017.05.087.

(9) Keller, L.; Ohs, B.; Lenhart, J.; Abduly, L.; Blanke, P.; Wessling, M. High Capacity Polyethylenimine Impregnated Microtubes Made of Carbon Nanotubes for CO_2 Capture. *Carbon N. Y.* **2018**, *126*, 338–345. https://doi.org/10.1016/j.carbon.2017.10.023.

(10) Chowdhury, S.; Balasubramanian, R. Three-Dimensional Graphene-Based Porous Adsorbents for Postcombustion CO_2 Capture. *Ind. Eng. Chem. Res.* **2016**, *55* (29), 7906–7916. https://doi.org/10.1021/acs.iecr.5b04052.

(11) Chowdhury, S.; Balasubramanian, R. Highly Efficient, Rapid and Selective CO_2 Capture by Thermally Treated Graphene Nanosheets. *J. CO2 Util.* **2016**, *13*, 50–60. https://doi.org/10.1016/j.jcou.2015.12.001.

(12) Chen, C.; Park, D. W.; Ahn, W. S. CO_2 Capture Using Zeolite 13X Prepared from Bentonite. *Appl. Surf. Sci.* **2014**, *292*, 63–67. https://doi.org/10.1016/j.apsusc.2013.11.064.

(13) Wang, L.; Yao, M.; Hu, X.; Hu, G.; Lu, J.; Luo, M.; Fan, M. Amine-Modified Ordered Mesoporous Silica: The Effect of Pore Size on CO_2 Capture Performance. *Appl. Surf. Sci.* **2015**, *324*, 286–292. https://doi.org/10.1016/j.apsusc.2014.10.135.

(14) Li, S.; Huo, F. Metal–Organic Framework Composites: From Fundamentals to Applications. *Nanoscale* **2015**, *7* (17), 7482–7501. https://doi.org/10.1039/C5NR00518C.

(15) James, S. L. Metal-Organic Frameworks. *Chem. Soc. Rev.* **2003**, *32* (5), 276. https://doi.org/10.1039/b200393g.

(16) Grissom, T. G.; Driscoll, D. M.; Troya, D.; Sapienza, N. S.; Usov, P. M.; Morris, A. J.; Morris, J. R. Molecular-Level Insight into CO_2 Adsorption on the Zirconium-Based Metal-Organic Framework, UiO-66: A Combined Spectroscopic and Computational Approach. *J. Phys. Chem. C* **2019**, *123* (22), 13731–13738. https://doi.org/10.1021/acs.jpcc.9b02513.

(17) Ghanbari, T.; Abnisa, F.; Wan Daud, W. M. A. A Review on Production of Metal Organic Frameworks (MOF) for CO_2 Adsorption. *Sci. Total Environ.* **2020**, *707*, 135090. https://doi.org/10.1016/j.scitotenv.2019.135090.

(18) Zhang, Y. H.; Bai, J.; Chen, Y.; Kong, X. J.; He, T.; Xie, L. H.; Li, J. R. A Zn(II)-Based Pillar-Layered Metal–Organic Framework: Synthesis, Structure, and CO_2 Selective Adsorption. *Polyhedron* **2019**, *158*, 283–289. https://doi.org/10.1016/j.poly.2018.10.067.

(19) Poloni, R.; Lee, K.; Berger, R. F.; Smit, B.; Neaton, J. B. Understanding Trends in CO_2 Adsorption in Metal-Organic Frameworks with Open-Metal Sites. *J. Phys. Chem. Lett.* **2014**, *5* (5), 861–865. https://doi.org/10.1021/jz500202x.

(20) Britt, D.; Furukawa, H.; Wang, B.; Glover, T. G.; Yaghi, O. M. Highly Efficient Separation of Carbon Dioxide by a Metal-Organic Framework Replete with Open Metal Sites. *Proc. Natl. Acad. Sci. U. S. A.* **2009**, *106* (49), 20637–20640. https://doi.org/10.1073/pnas.0909718106.

(21) Patel, H. A.; Yavuz, C. T. Noninvasive Functionalization of Polymers of Intrinsic Microporosity for Enhanced CO_2 capture. *Chem. Commun.* **2012**, *48* (80), 9989–9991. https://doi.org/10.1039/c2cc35392j.

(22) Liu, X. T.; Jia, Y. Y.; Zhang, Y. H.; Ren, G. J.; Feng, R.; Zhang, S. Y.; Zaworotko, M. J.; Bu, X. H. A New Co(Ii) Metal-Organic Framework with Enhanced CO_2 Adsorption and Separation Performance. *Inorg. Chem. Front.* **2016**, *3* (12), 1510–1515. https://doi.org/10.1039/c6qi00191b.

(23) Schneemann, A.; Bon, V.; Schwedler, I.; Senkovska, I.; Kaskel, S.; Fischer, R. A. Flexible Metal-Organic Frameworks. *Chem. Soc. Rev.* **2014**, *43* (16), 6062–6096. https://doi.org/10.1039/c4cs00101j.

(24) Chang, Z.; Yang, D. H.; Xu, J.; Hu, T. L.; Bu, X. H. Flexible Metal-Organic Frameworks: Recent Advances and Potential Applications. *Adv. Mater.* **2015**, *27* (36), 5432–5441. https://doi.org/10.1002/adma.201501523.

(25) Bhattacharyya, S.; Chakraborty, A.; Hazra, A.; Maji, T. K. Tetracarboxylate Linker-Based Flexible Cu II Frameworks: Efficient Separation of CO_2 from CO_2/N_2 and C_2H_2 from C_2H_2/C_2H_4 Mixtures. *ACS Omega* **2018**, *3* (2), 2018–2026. https://doi.org/10.1021/acsomega.7b01964.

(26) Xuan, Z. H.; Zhang, D. S.; Chang, Z.; Hu, T. L.; Bu, X. H. Targeted Structure Modulation of “Pillar-Layered” Metal-Organic Frameworks for CO_2 Capture. *Inorg. Chem.* **2014**, *53* (17), 8985–8990. https://doi.org/10.1021/ic500905z.

(27) Burnett, B. J.; Choe, W. Stepwise Pillar Insertion into Metal-Organic Frameworks: A Sequential Self-Assembly Approach. *CrystEngComm* **2012**, *14* (19), 6129–6131. https://doi.org/10.1039/c2ce25545f.

(28) Kitagawa, S.; Uemura, K. Dynamic Porous Properties of Coordination Polymers Inspired by

Hydrogen Bonds. *Chem. Soc. Rev.* **2005**, *34* (2), 109–119. https://doi.org/10.1039/b313997m.

(29) Zarekarizi, F.; Joharian, M.; Morsali, A. Pillar-Layered MOFs: Functionality, Interpenetration, Flexibility and Applications. *J. Mater. Chem. A* **2018**, *6* (40), 19288–19329. https://doi.org/10.1039/c8ta03306d.

(30) Chang, Z.; Zhang, D. S.; Chen, Q.; Li, R. F.; Hu, T. L.; Bu, X. H. Rational Construction of 3D Pillared Metal-Organic Frameworks: Synthesis, Structures, and Hydrogen Adsorption Properties. *Inorg. Chem.* **2011**, *50* (16), 7555–7562. https://doi.org/10.1021/ic2004485.

(31) Healy, C.; Patil, K. M.; Wilson, B. H.; Hermanspahn, L.; Harvey-Reid, N. C.; Howard, B. I.; Kleinjan, C.; Kolien, J.; Payet, F.; Telfer, S. G.; et al. The Thermal Stability of Metal-Organic Frameworks. *Coord. Chem. Rev.* **2020**, *419*, 213388. https://doi.org/10.1016/j.ccr.2020.213388.

(32) Li, N.; Xu, J.; Feng, R.; Hu, T. L.; Bu, X. H. Governing Metal-Organic Frameworks towards High Stability. *Chem. Commun.* **2016**, *52* (55), 8501–8513. https://doi.org/10.1039/c6cc02931k.

(33) Bosch, M.; Zhang, M.; Zhou, H.-C. Increasing the Stability of Metal-Organic Frameworks. *Adv. Chem.* **2014**, *2014*, 1–8. https://doi.org/10.1155/2014/182327.

(34) Ding, M.; Cai, X.; Jiang, H. L. Improving MOF Stability: Approaches and Applications. *Chem. Sci.* **2019**, *10* (44), 10209–10230. https://doi.org/10.1039/c9sc03916c.

(35) Tomar, K.; Verma, A.; Bharadwaj, P. K. Exploiting Dimensional Variability in Cu Paddle-Wheel Secondary Building Unit Based Mixed Valence Cu(II)/Cu(I) Frameworks from a Bispyrazole Ligand by Solvent/PH Variation. *Cryst. Growth Des.* **2018**, *18* (4), 2397–2404. https://doi.org/10.1021/acs.cgd.8b00002.

(36) Sheldrick, G. M. SHELXT - Integrated Space-Group and Crystal-Structure Determination. *Acta Crystallogr. Sect. A Found. Crystallogr.* **2015**, *71* (1), 3–8. https://doi.org/10.1107/S2053273314026370.

(37) Sheldrick, G. M. Crystal Structure Refinement with SHELXL. *Acta Crystallogr. Sect. C Struct. Chem.* **2015**, *71* (Md), 3–8. https://doi.org/10.1107/S2053229614024218.

(38) Dolomanov, O. V.; Bourhis, L. J.; Gildea, R. J.; Howard, J. A. K.; Puschmann, H. OLEX2: A Complete Structure Solution, Refinement and Analysis Program. *J. Appl. Crystallogr.* **2009**, *42* (2), 339–341. https://doi.org/10.1107/S0021889808042726.

(39) Chiang, Y. C.; Yeh, C. Y.; Weng, C. H. Carbon Dioxide Adsorption on Porous and Functionalized Activated Carbon Fibers. *Appl. Sci.* **2019**, *9* (10). https://doi.org/10.3390/app9101977.

(40) Dyall, Kenneth G.; Knut, F. J. *Introduction to Relativistic Quantum Chemistry*, Oxford Uni.; New York, 2007.

(41) Te Velde, G.; Bickelhaupt, F. M.; Baerends, E. J.; Fonseca Guerra, C.; van Gisbergen, S. J. A.; Snijders, J. G.; Ziegler, T. Chemistry with ADF. *J. Comput. Chem.* **2001**, *22* (9), 931–967. https://doi.org/10.1002/jcc.1056.

(42) Vrije Universiteit. Amsterdam Density Functional (ADF) Code, Release 2014. Amsterdam, The Netherlands 2018.

(43) Van Lenthe, E.; Baerends, E. J.; Snijders, J. G. Relativistic Total Energy Using Regular

Approximations. *J. Chem. Phys.* **1994**, *101* (11), 9783–9792. https://doi.org/10.1063/1.467943.

(44) Filatov, M.; Cremer, D. On the Physical Meaning of the ZORA Hamiltonian. *Mol. Phys.* **2003**, *101* (14), 2295–2302. https://doi.org/10.1080/0026897031000137670.

(45) Faas, S.; Snijders, J. G.; van Lenthe, J. H.; van Lenthe, E.; Baerends, E. J. The ZORA Formalism Applied to the Dirac-Fock Equation. *Chem. Phys. Lett.* **1995**, *246* (6), 632–640. https://doi.org/10.1016/0009-2614(95)01156-0.

(46) Van Lenthe, E.; Baerends, E. J. Optimized Slater-Type Basis Sets for the Elements 1-118. *J. Comput. Chem.* **2003**, *24* (9), 1142–1156. https://doi.org/10.1002/jcc.10255.

(47) Hammer, B.; Hansen, L. B.; Nørskov, J. K. Improved Adsorption Energetics within Density-Functional Theory Using Revised Perdew-Burke-Ernzerhof Functionals. *Phys. Rev. B - Condens. Matter Mater. Phys.* **1999**, *59* (11), 7413–7421. https://doi.org/10.1103/PhysRevB.59.7413.

(48) Allouche, A. Software News and Updates Gabedit — A Graphical User Interface for Computational Chemistry Softwares. *J. Comput. Chem.* **2012**, *32*, 174–182. https://doi.org/10.1002/jcc.

(49) Versluis, L.; Ziegler, T. The Determination of Molecular Structures by Density Functional Theory. The Evaluation of Analytical Energy Gradients by Numerical Integration. *J. Chem. Phys.* **1988**, *88* (1), 322–328. https://doi.org/10.1063/1.454603.

(50) Cukrowski, I.; De Lange, J. H.; Mitoraj, M. Physical Nature of Interactions in ZnII Complexes with 2,2′-Bipyridyl: Quantum Theory of Atoms in Molecules (QTAIM), Interacting Quantum Atoms (IQA), Noncovalent Interactions (NCI), and Extended Transition State Coupled with Natural Orbitals for Chemical . *J. Phys. Chem. A* **2014**, *118* (3), 623–637. https://doi.org/10.1021/jp410744x.

(51) Thommes, M.; Kaneko, K.; Neimark, A. V.; Olivier, J. P.; Rodriguez-Reinoso, F.; Rouquerol, J.; Sing, K. S. W. Physisorption of Gases, with Special Reference to the Evaluation of Surface Area and Pore Size Distribution (IUPAC Technical Report). *Pure Appl. Chem.* **2015**, *87* (9–10), 1051–1069. https://doi.org/10.1515/pac-2014-1117.

(52) Sing, K. S. W. Reporting Physisorption Data for Gas/Solid Systems with Special Reference to the Determination of Surface Area and Porosity (Recommendations 1984). *Pure Appl. Chem.* **1985**, *57* (4), 603–619. https://doi.org/10.1351/pac198557040603.

(53) Liu, Q.; Ning, L.; Zheng, S.; Tao, M.; Shi, Y.; He, Y. Adsorption of Carbon Dioxide by MIL-101(Cr): Regeneration Conditions and Influence of Flue Gas Contaminants. *Sci. Rep.* **2013**, *3*, 1–6. https://doi.org/10.1038/srep02916.

(54) Ahrenholtz, S. R.; Landaverde-Alvarado, C.; Whiting, M.; Lin, S.; Slebodnick, C.; Marand, E.; Morris, A. J. Thermodynamic Study of CO_2 Sorption by Polymorphic Microporous MOFs with Open Zn(II) Coordination Sites. *Inorg. Chem.* **2015**, *54* (9), 4328–4336. https://doi.org/10.1021/ic503047y.

(55) Lin, R. B.; Chen, D.; Lin, Y. Y.; Zhang, J. P.; Chen, X. M. A Zeolite-like Zinc Triazolate Framework with High Gas Adsorption and Separation Performance. *Inorg. Chem.* **2012**, *51* (18), 9950–9955. https://doi.org/10.1021/ic301463z.

(56) Farrusseng, D.; Daniel, C.; Gaudillère, C.; Ravon, U.; Schuurman, Y.; Mirodatos, C.; Dubbeldam, D.; Frost, H.; Snurr, R. Q. Heats of Adsorption for Seven Gases in Three Metal - Organic Frameworks: Systematic Comparison of Experiment and Simulation. *Langmuir* **2009**, *25* (13),

7383–7388. https://doi.org/10.1021/la900283t.

(57) Zhai, Q. G.; Bu, X.; Mao, C.; Zhao, X.; Daemen, L.; Cheng, Y.; Ramirez-Cuesta, A. J.; Feng, P. An Ultra-Tunable Platform for Molecular Engineering of High-Performance Crystalline Porous Materials. *Nat. Commun.* **2016**, *7*, 1–9. https://doi.org/10.1038/ncomms13645.

(58) Zhai, Q. G.; Bu, X.; Zhao, X.; Li, D. S.; Feng, P. Pore Space Partition in Metal-Organic Frameworks. *Acc. Chem. Res.* **2017**, *50* (2), 407–417. https://doi.org/10.1021/acs.accounts.6b00526.

(59) Mason, J. A.; Sumida, K.; Herm, Z. R.; Krishna, R.; Long, J. R. Evaluating Metal-Organic Frameworks for Post-Combustion Carbon Dioxide Capture via Temperature Swing Adsorption. *Energy Environ. Sci.* **2011**, *4* (8), 3030–3040. https://doi.org/10.1039/c1ee01720a.

(60) Hu, J.; Liu, Y.; Liu, J.; Gu, C.; Wu, D. High CO_2 Adsorption Capacities in UiO Type MOFs Comprising Heterocyclic Ligand. *Microporous Mesoporous Mater.* **2018**, *256*, 25–31. https://doi.org/10.1016/j.micromeso.2017.07.051.